Estimating Ice Water Content for Winter Storms from Millimeter-Wavelength Radar Measurements Using a Synthesis of Polarimetric and Dual-Frequency Radar Observations

MARIKO OUE,[a] ALEXANDER V. RYZHKOV,[b,c] SERGEY Y. MATROSOV,[d,e] PETAR BUKOVČIĆ,[b,c] AND PAVLOS KOLLIAS[a,f]

[a] *School of Marine and Atmospheric Sciences, Stony Brook University, State University of New York, Stony Brook, New York*
[b] *NOAA National Severe Storms Laboratory, Norman, Oklahoma*
[c] *Cooperative Institute for Severe and High-Impact Weather Research and Operations, University of Oklahoma, Norman, Oklahoma*
[d] *Cooperative Institute for Research in Environmental Sciences, University of Colorado Boulder, Boulder, Colorado*
[e] *NOAA Physical Sciences Laboratory, Boulder, Colorado*
[f] *Environmental and Climate Sciences Department, Brookhaven National Laboratory, Upton, New York*

(Manuscript received 25 October 2023, in final form 22 October 2024, accepted 28 October 2024)

ABSTRACT: The potential of millimeter-wavelength radar-based ice water content (IWC) estimation is demonstrated using a Ka-band Scanning Polarimetric Radar (KASPR) for the U.S. northeast coast winter storms. Two IWC relations for Ka-band polarimetric radar measurements are proposed: one that uses a combination of the radar reflectivity Z and the estimated total number concentration of snow particles N_t and the other based on the joint use of Z, specific differential phase K_{DP}, and the degree of riming f_{rim}. A key element of the algorithms is to obtain the "Rayleigh-equivalent" value of Z measured at the Ka band, i.e., the corresponding Z at a longer radar wavelength for which Rayleigh scattering takes place. This is achieved via polarimetric retrieval of the mean volume diameter D_m and incorporating the relationship between the dual-wavelength ratio $DWR_{S/Ka}$ and D_m. Those techniques allow for retrievals from single millimeter-wavelength radar measurements and do not necessarily require the dual-wavelength ratio (DWR) measurements, if the DWR–D_m relation and Rayleigh assumption for Ka-band K_{DP} are valid. Comparison between the quasivertical profile product obtained from KASPR and the columnar vertical profile product generated from the nearby WSR-88D S-band radar measurements demonstrates that the $DWR_{S/Ka}$ can be estimated from the two close radars without the need for collocated radar beams and synchronized antenna scanning and can be used for determining the Rayleigh-equivalent value of Z. The performance of the suggested techniques is evaluated for seven winter storms using surface disdrometer and snow accumulation measurements.

SIGNIFICANCE STATEMENT: Ice water content (IWC) estimation using millimeter-wavelength radar measurements has been challenging for decades, because of the complexity of snow particle properties and size, which can cause complex scattering at the shorter radar wavelengths. The suggested polarimetric techniques overcome this difficulty via utilizing specific differential phase K_{DP} which is higher at millimeter wavelengths than at centimeter wavelengths. This study proposes new IWC relationships for Ka-band polarimetric radar measurements and evaluates them using a Ka-band Scanning Polarimetric Radar (KASPR) and a nearby NEXRAD (S-band) polarimetric radar for the U.S. northeast coast winter storms. The proposed techniques can be applied to other millimeter-wavelength radars and shed light on the millimeter-wavelength polarimetric radar IWC estimation.

KEYWORDS: Snow; Cloud retrieval; Radars/Radar observations

1. Introduction

Modern weather radar operational networks provide observables for quantitative precipitation estimation (QPE) over broad areas. While significant progress in estimating liquid precipitation has been achieved recently after the introduction and widespread utilization of polarimetric radars (e.g., Ryzhkov et al. 2022), reliable QPE during ice and snow conditions remains a challenge due to the complexity and wide diversity of the microphysical properties of ice (e.g., Sekhon and Srivastava 1970; Ryzhkov et al. 1998; Matrosov et al. 2019; Szyrmer et al. 2012; Heymsfield et al. 2013; Huang et al. 2015; von Lerber et al. 2017). Weather services are mainly interested in reliable estimation of snow intensity commonly characterized by the snow water equivalent, whereas robust estimates of ice water content (IWC), characteristic size of snowflakes (often quantified by their mean volume diameter D_m), and their total number concentration N_t are needed to optimize the performance of numerical weather prediction (NWP) models. Such estimates will also be useful for evaluating the representation of Earth's hydrological cycle in global circulation and climate models (Stephens et al. 1990; IPCC 2013).

For the quantification of ice and snow, numerous empirical equations that are optimized for snow type and location have been proposed. For instance, for IWC and snow rate S estimates, a power-law form using radar reflectivity has been commonly utilized, where the coefficients in the relationships

Corresponding author: Mariko Oue, mariko.oue@stonybrook.ed

DOI: 10.1175/JTECH-D-23-0143.1

significantly vary with snow types and location (e.g., Hogan et al. 2006; Matrosov and Heymsfield 2017; references listed in Bukovčić et al. 2018). Quantification of ice and snow can be significantly improved using polarimetric and/or Doppler radar measurements, which provide capabilities of accounting for the snow particle properties and size distribution parameters (e.g., Matrosov et al. 2002; Maahn and Loehnert 2017; Bukovčić et al. 2018). Bukovčić et al. (2018) proposed a polarimetric approach for estimating IWC and snow rate at the S band, i.e., at the radar wavelengths between 10 and 11 cm. The polarimetric relations were derived using large datasets of disdrometer measurements of snow. These relations have been validated by Bukovčić et al. (2020) using polarimetric radar measurements for several snowstorms.

Another important development facilitating a better understanding of the microphysical processes of snow formation and its quantification was the introduction of the quasivertical profile (QVP) methodology for processing and visualization of the polarimetric radar data collected in storms of predominantly stratiform nature (Kumjian et al. 2013; Ryzhkov et al. 2016). The QVP technique implies azimuthal averaging of the radar data at higher elevations and projecting the resulting averages onto the vertical so that the polarimetric radar data are represented in a height-versus-time format. Such a format is similar to the one in the data from the vertically pointing radars operating at different microwave frequencies that are traditionally displayed. This makes it very convenient to compare and integrate polarimetric and multifrequency radar data. The original QVP methodology was further expanded and modified to obtain the so-called range-defined QVPs (RD-QVPs) (Tobin and Kumjian 2017) and the columnar vertical profiles (CVPs) (Murphy et al. 2020; Bukovčić et al. 2017—enhanced vertical profiles (EVPs) extended spatially and rebranded later as CVP). As opposed to QVP (or RD-QVP) which is a radar-centric domain averaging product, the CVP represents the polarimetric radar variables within the vertical column in a smaller horizontal domain compared to the QVP averaging area which can be at any location with respect to the radar.

Over the last two decades, millimeter-wavelength (cloud) radar observations of clouds and precipitation have become routine (e.g., Kollias et al. 2014a,b; Löhnert et al. 2015; Oue et al. 2018, 2021; Kollias et al. 2020a). Due to their short wavelength, cloud radars generally have higher sensitivities to smaller ice particles and higher spatial resolution compared to the operational surveillance centimeter-wavelength radars (Kollias et al. 2007). For the cloud radar observations, power-law relationships between IWC and radar reflectivity Z with constants a and b, i.e., IWC $= aZ^b$, have been commonly used (e.g., Hogan et al. 2006; Matrosov and Heymsfield 2017). The coefficients need to be optimized carefully for snow types and locations.

Past studies on microphysical snow retrievals using millimeter-wavelength cloud radars capitalized on the non-Rayleigh scattering characteristics to quantify the snow properties (e.g., Aydin and Walsh 1999; Botta et al. 2011). For instance, they used dual-wavelength ratio (DWR) of radar reflectivities at two (or three) different wavelengths to obtain particle size information (e.g., Hogan et al. 2006; Heymsfield et al. 2016; Matrosov et al. 2019, 2022; Mroz et al. 2021; Tetoni et al. 2022), liquid water content (e.g., Hogan et al. 2005; Huang et al. 2009; Tridon et al. 2013; Zhu et al. 2019), ice water content, snowfall rate (e.g., Matrosov 1998; Tetoni et al. 2022), and identification of particle types (e.g., Kneifel et al. 2015; Leinonen and Moisseev 2015; Leinonen and Szyrmer 2015; Moisseev et al. 2015; Sinclair et al. 2016; Matrosov et al. 2020). In addition to DWR, polarimetric capabilities of the cloud radars can further improve snow quantification (e.g., Matrosov et al. 2017; Kollias et al. 2020a; Matrosov 2021; Oue et al. 2021).

The Stony Brook Radar Observatory (SBRO) has operated a millimeter-wavelength radar facility since 2017 (40.890°N, 73.127°W; Kollias et al. 2020b; Oue et al. 2021) including a Ka-band Scanning Polarimetric Radar (KASPR), which is located about 22 km away from the National Weather Service Next Generation Weather Radar (NEXRAD) S-band polarimetric radar at Upton, New York [Weather Surveillance Radar-1988 Doppler (WSR-88D); named KOKX, 40.866°N, 72.864°W]. These two radars are sufficiently close for utilizing their QVP/CVP products and the dual-wavelength ratio to compare the snow microphysical observations at the S and Ka bands. In this study, two techniques to estimate IWC from the Ka-band polarimetric radar measurements are proposed in conjunction with the dual-wavelength radar measurements using the NEXRAD S-band radar. Using certain assumptions on bulk particle shape and size distributions, these techniques avoid the need for complicated scattering calculations that account for complex particle habits or densities. The paper is organized as follows: Section 2 introduces the observation strategies and data processing; section 3 describes the theory to derive the equations for the IWC estimates; section 4 demonstrates how the theory is applied to our datasets; section 5 shows and discusses the IWC estimate results, and section 6 summarizes the results of this study.

2. Data

a. KASPR

KASPR is a 35-GHz scanning polarimetric cloud radar with the alternate transmission of horizontally (h) and vertically (v) polarized waves and simultaneous reception of copolar and cross-polar components of the backscattered wave with a beamwidth of 0.32°, capable of measuring a full set of polarimetric radar observables including radar reflectivity at horizontal polarization Z_{hh}, differential reflectivity Z_{DR}, differential phase φ_{DP}, copolar correlation coefficient ρ_{hv}, linear depolarization ratio L_{DR}, and cross-polar correlation coefficient ρ_{hx}, along with Doppler velocity and spectral width. Specific differential phase K_{DP} is estimated using an iterative algorithm proposed by Hubbert and Bringi (1995). The data postprocessing details are described in Oue et al. (2018). The KASPR was calibrated using a corner reflector technique. The detailed configurations are also described in Kumjian et al. (2020) and Kollias et al. (2020b).

KASPR executed a scanning strategy that consisted of plan position indicator (PPI) scans at 15° (and 20° for the 2018

case) elevation angle, a zenith pointing PPI, hemispheric range–height indicator (HSRHI) scans, and a vertically pointing (VPT) mode. This pattern was repeated and took approximately 13–15 min to complete. During a cycle, two 15° PPI scans were included, so that we had the tilted PPI scans every ~7 min which were used to produce QVP (Kumjian and Lombardo 2017; Ryzhkov et al. 2016) products. Since the slant range resolution of the PPI data is 30 m, the corresponding vertical spacing of the QVP data is about 7.8 m. Note that the actual vertical resolution of QVP is determined by the vertical size of the radar resolution volume, which increases with the distance from the radar (Ryzhkov et al. 2016). This study mainly uses the QVP product using the data collected at the 15° PPI scans.

All scans in 2017 and 2018 and VPT scans from 2019 to 2021 were operated with a short pulse mode, resulting in the KASPR maximum observation range of 30 km with the minimum detectable reflectivity of −5 dBZ. The PPI and HSRHI scans were operated with a pulse compression, resulting in the maximum range of 29 km with the minimum detectable reflectivity of −27 dBZ.

b. WSR-88D radar

We used the data from the NEXRAD WSR-88D radar multiangle PPI scans at the OKX site (named KOKX). The KOKX PPI data are used to construct the CVPs as described in Murphy et al. (2020) to be compared with KASPR QVPs. The KOKX data were averaged over a 10 km × 10 km horizontal CVP domain centered around the KASPR location with a vertical resolution of 50 m. We used data from all elevation angles from each volume coverage pattern every approximately 5 min. The height–time data from the KOKX CVP are linearly interpolated into the KASPR QVP height–time domain to obtain $DWR_{S/Ka}$. Note that KOKX did not have higher elevation PPI scans to cover the entire cloud depths for all cases.

c. Ground-based in situ measurements

An over-the-top (OTT) Parsivel^2 optical disdrometer (Parsivel hereafter) was collocated with KASPR in SBRO since 2017. It measures the terminal velocity and diameter of individual precipitation particles passing through a sheet of a 650-nm laser diode light (30 mm wide, 1 mm high, and 180 mm long) with a power of 3 mW (Löffler-Mang and Blahak 2001). The total measuring surface has an area of 54 cm^2. The measured particle diameter and velocity are classified into one of 32 diameter bins ranging from 0.062 to 24.5 mm in diameter and 32 velocity bins ranging from 0.04 to 20.5 m s^{-1} every 1 min. A Parsivel built-in OTT Application Software for Data Observation (ASDO) software estimates precipitation rate based on the measured size, number, and fall speeds. We resampled and integrated the number of particles every 5 min to reduce noisiness.

An OTT Pluvio^2 L precipitation weighing gauge (Pluvio hereafter) was also collocated next to the Parsivel since 2019. It has a 400-cm^2 collecting area with an integrated orifice rim heater and measures the mass of precipitation every minute. We resampled and integrated the precipitation data every 5 min.

Snowflake photos from surface cameras were used for qualitative evaluation and understanding of the cases. The multiangle snowflake camera (MASC; Garrett et al. 2012, Garrett and Yuter 2014) was located adjacent to the Parsivel disdrometer. The MASC did not work for all cases due to mechanical issues, and we took complementary photos of snowflakes using a single-lens reflex (SLR) camera.

d. Soundings and weather station

We used twice-a-day sounding data at 0000 and 1200 UTC from the nearest NWS site, OKX. In addition to the NWS soundings, we performed sounding measurements using the Graw Radiosondes (GRAW) sounding system installed on a mobile radar truck in 2020 and 2021. The GRAW soundings were performed to complement the NWS soundings such that we could have the sounding data approximately every 3 h. The mobile radar truck was deployed in several locations near Stony Brook including Cedar Beach (40.965°N, 73.030°W; 18 January 2020) and Stony Brook University (40.897°N, 73.127°W; on 17 December 2020 and 1 February 2021). A weather station operated by the Stony Brook University (SBU) School of Marine and Atmospheric Sciences near the KASPR site (40.895°N, 73.124°W) is used to check the surface temperature.

3. Theory

a. IWC equations in the Rayleigh scattering regime

1) IWC(N_T, Z, μ)

Various IWC(Z) relations have been proposed in the past (e.g., Bukovčić et al. 2018). Delanoë et al. (2014) and Bukovčić et al. (2018) examined large datasets of in situ aircraft and surface disdrometer measurements of ice/snow particle size distribution (PSD) and demonstrated that the multiplier a in the power-law relation IWC = aZ^b is a strong function of the intercept N_{0s} if the PSD is fitted to the exponential size distribution $N(D) = N_{0s}\exp(-\Lambda D)$.

It can be shown that the multiplier in the IWC(Z) relation is also a function of the total number concentration of ice particles N_t. Furthermore, if a gamma-function PSD is assumed, the relation between IWC, Z, and N_t can be found in Huang et al. [2021; their Eq. (A16)]:

$$Z = 8.17 \times 10^2 f(\mu)\frac{\mathrm{IWC}^2}{N_t}, \tag{1}$$

where

$$f(\mu) = \frac{\Gamma(5+\mu)\Gamma(1+\mu)}{[\Gamma(3+\mu)]^2}, \tag{2}$$

where μ is the shape parameter of the gamma function $N(D) = N_0 D^{\mu} e^{-\Lambda D}$. In Eq. (1), Z is the reflectivity factor (mm^6 m^{-3}), IWC is expressed in grams per cubic meter, and N_t is expressed in per liter (L^{-1} or m^{-3}/10^3). Equation (1) was

theoretically derived in the Rayleigh scattering approximation assuming that the bulk density of a snowflake ρ_s is inversely proportional to its equivolume diameter D (Zawadzki et al. 2005; Ryzhkov and Zrnić 2019) as

$$\rho_s = \alpha_0 f_{\text{rim}} D^{-1}, \tag{3}$$

where α_0 is a constant, which is approximately equal to 0.15, and $f_{\text{rim}} > 1$ is the degree of riming, which is equal to 1 for unrimed snow. In Eq. (3), ρ_s is expressed in grams per cubic centimeter and D is expressed in millimeters. The degree of riming f_{rim} is dimensionless and is related to the rime mass fraction FR as $f_{\text{rim}} = 1/(1 - \text{FR})$, where FR is the ratio of the rime mass m_{rime} to the snowflake mass (FR $= m_{\text{rime}}/m$) (Moisseev et al. 2017).

The Eq. (1) was derived using integration of Z, IWC, and N_t over gamma PSD with diameters ranging from 0 to ∞ which results in an analytical solution that is very sensitive to the value of the shape parameter μ. The factor $f(\mu)$ and the total concentration N_t become infinite for $\mu = -1$ which is unphysical. It can be concluded from the previous studies (e.g., Tiira et al. 2016; Matrosov and Heymsfield 2017; Duffy and Posselt 2022) that μ is close to zero in the dendritic growth layer (DGL) centered at $T = -15$°C but tends to be negative reaching values -2 at $T = 0$°C close to the surface where snow is more aggregated.

To constrain the value of $f(\mu)$ for negative μ, we performed integration of Z, IWC, and N_t numerically in the size interval between 0.1 and 20 mm given the fact that ice particles with sizes below 0.1 mm contribute very little to Z and IWC. In our simulations, we also cap the snow density ρ_s by the value 0.917 g cm^{-3} to prevent unrealistically high values of ρ_s in Eq. (3) for $f_{\text{rim}} > 1$. Computing the ratio IWC/$(ZN_t)^{1/2}$ as a function of μ and approximating it with a polynomial yield a relation:

$$\text{IWC}(N_t, Z, \mu) = 0.0147 f_0(\mu) N_t^{0.5} Z^{0.5}, \tag{4}$$

where

$$f_0(\mu) = 1 + 0.33\mu - 0.043\mu^2, \tag{5}$$

if $-2 < \mu < 3$. The function $f_0(\mu)$ is much less sensitive to μ compared to $f(\mu)$ and can be used for $\mu \leq -1$. One of the important advantages of Eq. (4) is that it is not sensitive to the variability of the degree of riming f_{rim}.

2) IWC(K_{DP}, Z, f_{rim})

Bukovčić et al. (2020) suggested a polarimetric relation for IWC that uses a combination of Z and K_{DP}. In our study, we will use the following IWC(K_{DP}, Z, f_{rim}) relation originating from the one in Bukovčić et al. (2020), derived from 16 snowstorms observed in Oklahoma:

$$\text{IWC}(K_{\text{DP}}, Z, f_{\text{rim}}) = 17.5 \times 10^{-3} (F_s F_o)^{-0.66} f_{\text{rim}}{}^{-0.94} (K_{\text{DP}}\lambda)^{0.66} Z^{0.28}, \tag{6}$$

where F_s and F_o are the particle shape and orientation factors, λ is the radar wavelength (mm), K_{DP} is expressed in degrees per kilometer, and Z is expressed in millimeters to the sixth power per cubic meter. In Eq. (6), $\alpha_0 = 0.15$ g cm^{-3} mm is used for the snow density relation [Eq. (3)]. Equation (6) is slightly different from Bukovčić et al. [2020; their Eq. (20)] with empirically optimized the exponent of f_{rim} (originally -1). The f_{rim} was estimated from the squared ratio of the disdrometer-measured terminal velocity to the empirically predetermined terminal velocity value, as described in Bukovčić et al. (2018) Eq. (7). The adjustment of f_{rim} was made based on the matching of the radar and the Automated Surface Observing System estimates of IWC for eight dry snow cases. For an average aspect ratio of snow particles of around 0.6 (e.g., Matrosov et al. 2020), $F_s = 0.214$ and $F_o = 0.7$ if the width of the canting angle distribution is equal to 20° (Ryzhkov and Zrnić 2019; Bukovčić et al. 2020). Under these assumptions,

$$\text{IWC}(K_{\text{DP}}, Z, f_{\text{rim}}) = 6.13 \times 10^{-2} f_{\text{rim}}^{-0.94} (K_{\text{DP}}\lambda)^{0.66} Z^{0.28}. \tag{7}$$

b. Adaptation of the equations for Rayleigh scattering to the Ka band

The radar reflectivity factor Z is determined by the largest particles in the size spectrum; thus, the Rayleigh scattering approximation generally cannot be used to estimate Z at the Ka band. In ice/snow conditions, attenuation at the Ka band from hydrometeors can be neglected, and the dual-wavelength ratio $\text{DWR}_{\text{S/Ka}}$ is a function of the snowflake's characteristic size and represents the departure of the Ka-band radar reflectivity Z_{Ka} from the one for Rayleigh scattering Z which is identical to the S-band radar reflectivity Z_{S}. In other words, $\text{dB}Z_{\text{S}} = \text{dB}Z_{\text{Ka}} + \text{DWR}_{\text{S/Ka}}$. We use theoretical simulations for a simple spheroidal model of snowflakes to obtain the dual-wavelength ratio $\text{DWR}_{\text{S/Ka}}$ as a function of the characteristic snowflake size. To obtain the $\text{DWR}_{\text{S/Ka}}$ as a function of snowflake size, we assume a particle mass m versus particle maximum dimension D_{max} relation given by von Lerber et al. (2017):

$$m = 3.65 \times 10^{-5} D_{\text{max}}^{2.1}. \tag{8}$$

The T-matrix computations of $\text{DWR}_{\text{S/Ka}}$ with median volume diameter D_{mv} up to ~3 mm and assuming a low elevation angle (15°, consistent with the KASPR QVP) yield the following dependence of the dual-wavelength ratio on the D_{mv} for an exponential PSD (see Fig. 1):

$$\text{DWR}_{\text{S/Ka}} = 0.91 D_{\text{mv}}^{1.73}. \tag{9}$$

In Eqs. (8) and (9), m is expressed in grams, D_{max} and D_{mv} are expressed in millimeters, and DWR is expressed in decibels. In the derivation of Eq. (9), it is assumed that the aspect ratio of a spheroidal snowflake is 0.6 at an elevation angle of 15°. Note that there is about 10% variability in the DWR–D_{mv} relation due to assumption about particle aspect ratio between 0.3 and 0.8 at this geometry. Also, note that DWR depends on particle density rather weakly (e.g., Matrosov 1998). The dual-wavelength ratio can also be determined from the mean volume diameter D_m which is the ratio of the fourth and third PSD

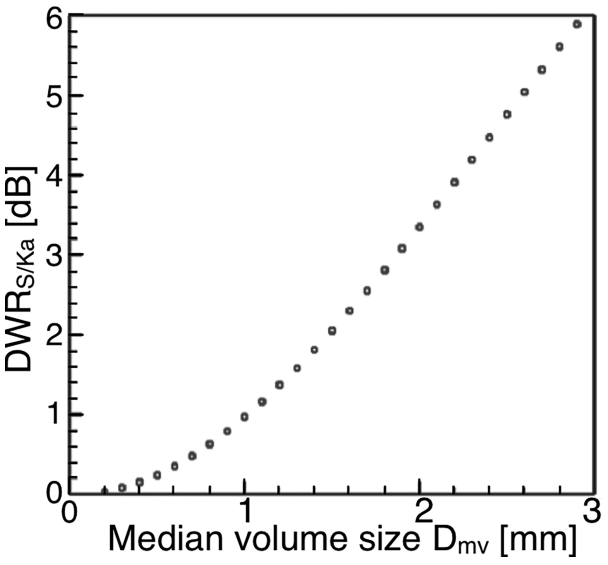

FIG. 1. $DWR_{S/Ka}$ vs D_{mv} from scattering calculations at an elevation angle of 15°.

moments. The terms D_m and D_{mv} are typically very close (e.g., Matrosov et al. 2022; $D_{mv} \sim 0.917\, D_m$ with $\mu = 0$). For simplicity, we assume that $D_{mv} \sim 0.917\, D_m$ and

$$\mathrm{DWR}_{S/Ka} \approx 0.78 D_m^{1.73}. \tag{10}$$

Note that the coefficient of the D_{mv}–D_m relation slightly changes with the μ value (approximately 0.01 between $\mu = -1$ and $\mu = 0$), and it changes the IWC estimates by <5%.

To obtain the estimate of D_m, we can utilize an equation (Ryzhkov and Zrnić 2019):

$$D_m = 0.67\left(\frac{Z}{K_{DP}\lambda}\right)^{1/3}, \tag{11}$$

which is applicable in the Rayleigh approximation and can be used at the S band but not at the Ka band. To derive D_m using measurements at the Ka band, we have to solve the following equation using polarimetric radar observables (i.e., K_{DP}):

$$D_m = 0.67\left(\frac{10^{0.1(\mathrm{dBZ_{Ka}}+0.78D_m^{1.73})}}{K_{DP}\lambda}\right)^{1/3}. \tag{12}$$

In Eq. (12), D_m and λ are expressed in millimeters and $\mathrm{dBZ_{Ka}}$ is the reflectivity (dBZ) at the Ka band. Equation (12) must be solved numerically for D_m using measured values of Z and K_{DP} at the Ka band. Once D_m is computed, the values of Z in the equations for IWC(N_t, Z, μ) and IWC(K_{DP}, Z, f_{rim}) should be replaced using the formula:

$$Z = 10^{0.1(\mathrm{dBZ_{Ka}}+0.78D_m^{1.73})}, \tag{13}$$

where $\mathrm{dBZ_{Ka}}$ is the measured radar reflectivity at the Ka band (dBZ).

The value of D_m can also be used together with Z for a rough estimation of N_t. In the Rayleigh approximation for the exponential size distribution and spherical shape of the snow particles (e.g., Bukovčić et al. 2018; Ryzhkov and Zrnić 2019),

$$Z = \frac{|K_i|^2}{|K_w|^2}\frac{1}{\rho_i^2}\int_0^\infty \rho_s^2(D)D^6N(D)dD = 2.12\times10^{-2}\alpha_0^2 f_{rim}^2 D_m^4 N_t, \tag{14}$$

where ρ_i is the density of ice, $|K_i|^2 = (\varepsilon_i - 1)^2/(\varepsilon_i + 2)^2$, and $|K_w|^2 = (\varepsilon_w - 1)2/(\varepsilon_w + 2)^2$, where ε_i and ε_w are dielectric constants of ice and liquid water, respectively. For $\alpha_0 = 0.15$, Eq. (14) gives

$$Z = 0.477 f_{rim}^2 N_t D_m^4. \tag{15}$$

Therefore, with Eq. (13),

$$N_t = 2.10 f_{rim}^{-2}\frac{Z}{D_m^4} = 2.10 f_{rim}^{-2}\frac{10^{0.1(\mathrm{dBZ_{Ka}}+0.78D_m^{1.73})}}{D_m^4}. \tag{16}$$

In Eq. (16), $\mathrm{dBZ_{Ka}}$ is in decibels, N_t is in per liter (L^{-1} or $m^{-3}/10^3$), and D_m is in millimeters.

This adaptation for the Ka band suggests that the IWC(N_t, Z, μ) and IWC(K_{DP}, Z, f_{rim}) estimates work with the Ka-band single-radar measurements once D_m is estimated from the Ka-band measurements using Eq. (13) (i.e., $DWR_{S/Ka}$ measurements are not necessary). We evaluate this adaptation using the $DWR_{S/Ka}$ measurements (section 4a).

A frequency dependency of K_{DP} should also be considered. Equations (4), (11), and (16) are valid for Rayleigh scatterers only; i.e., they are fully applicable at the S band but not at the Ka band. Because the K_{DP} of snowflakes is proportional to the first moment of PSD (unless the snow is heavily rimed) and is dominated by the contribution of smaller ice particles at the lower end of the size spectrum, K_{DP} at the Ka band is not much affected by the largest snowflakes at the higher end of the spectrum and can be estimated in the Rayleigh approximation. Matrosov (2021) showed that in Ka- and W-band radar measurements, non-Rayleigh scattering effects in K_{DP} were not very pronounced even at high radar frequencies for larger signal-to-noise ratios, and K_{DP} values scaled by the radar frequency from the two-frequency radars were well matched. Therefore, K_{DP} at the Ka band is equal to the wavelength-scaled K_{DP} at the S band: $K_{DPKa} = \lambda_S/\lambda_{Ka} \times K_{DPS} = 12.3K_{DPS}$ for $\lambda_S = 10.43$ cm and $\lambda_{Ka} = 0.85$ cm. This means that the product $K_{DP}\lambda$ in Eqs. (7) and (12) is approximately the same at the S and Ka bands. Direct proportionality between K_{DPKa} and K_{DPS} was demonstrated using the comparison of K_{DP} measured by the S-band KOKX WSR-88D and Ka-band KASPR radars in section 4a of this article.

In a nutshell, using Eqs. (12) and (13) and K_{DP} measured at the Ka band, the Eqs. (4) and (7) for IWC(N_t, Z, μ) and IWC(K_{DP}, Z, f_{rim}) can be utilized at the Ka band. We highlight that those IWC(N_t, Z, μ) and IWC(K_{DP}, Z, f_{rim}) estimates do not necessarily require $DWR_{S/Ka}$ measurements, once D_m is estimated from Eq. (12), if the DWR–D_m relation

TABLE 1. Sample size of data used in this study and mean surface temperature. Maximum and minimum surface temperatures are listed in parentheses.

Case	Period	No. of KASPR QVPs		No. of KOKX CVPs	Parsivel availability	Pluvio availability	Mean surface temp (max, min) (°C)
		Z only	Polarimetry available				
9 Dec 2017	1400–2130 UTC	58	57	69	Yes	No	−0.1 (2.2, −1.1)
14 Dec 2017	0530–1530 UTC	73	72	71	Yes	No	−4.2 (−3.2, −5.8)
4 Jan 2018	1000–2359 UTC	113	112	155	Yes	No	−4.1 (−3.2, −5.2)
20 Feb 2019	1730–2305 UTC	43	41	39	Yes	Yes	−3.3 (−2.3, −3.9)
18 Jan 2020	1800–2400 UTC	51	50	48	Yes	Yes	−3.1 (0.1, −3.7)
16–17 Dec 2020	2030–0300 UTC	57	56	55	Yes	Yes	−1.9 (1.1, −2.7)
1 Feb 2021	0200–2400 UTC	91	90	187	Yes	Yes	−2.1 (0, −5.7)

[Eq. (10)] and Rayleigh assumption for Ka-band K_{DP} are valid, and the values μ [for IWC(N_t, Z, μ)] and f_{rim} [for IWC(K_{DP}, Z, f_{rim})] are reasonably estimated or assumed.

4. Data processing

We apply the IWC estimates from the Ka-band radar measurements described in the previous section for the selected seven snowstorm cases from 2017 to 2021 winter observations. Table 1 lists the cases. We selected four cases where KASPR QVP, Parsivel, and Pluvio measurements were available for more than 6 h for each case from the 2019–21 winter seasons. Three more cases where KASPR QVP and Parsivel measurements were available from the 2017–18 winter season were added to the dataset. We excluded rain, mixed-phase, sleet, or frozen rain cases to avoid possible attenuation of the KASPR radar signal. Table 1 also shows the surface temperatures observed by a meteorological station at the radar site. Herein, we describe methods of preprocessing observation data that are applied to the theory.

a. KASPR and KOKX

We use KASPR QVP and KOKX CVP for the IWC retrievals in this study. This technique makes the comparisons of the data collected by two scanning radars located in different places easy in the same height-versus-time format. The KASPR QVPs are also used to estimate $D_m(K_{DP}, Z)$ using Eq. (12).

Figures 2 and 3 illustrate the comparison of the KASPR QVP and KOKX CVP in terms of Z and K_{DP} for the heavy snow event observed on 4 January 2018. The similarity of the vertical structure and evolution of the storm observed by noncollocated radars is remarkable. In areas of low Z, the radar reflectivity factors are very close, whereas substantial differences are observed where Z_S is high. This is also evident in Fig. 3a where the time series of the KASPR and KOKX values of Z measured at the height of 1 km is displayed. The two curves are almost indistinguishable when $dBZ_S < 20$ dBZ and deviate dramatically for higher Z_S where the difference between dBZ_S and dBZ_{Ka} (or DWR) reaches almost 20 dB. This occurs at about 2100 UTC when the size and total concentration of snowflakes are maximal as is shown in Fig. 3c. This feature is repetitive as can be seen in Fig. 4a, which is a KASPR Z versus KOKX Z distribution for all seven cases. The KASPR Z and KOKX Z are well matched for $Z < 20$ dBZ, and their difference starts increasing for KOKX $Z > 20$ dBZ. This means that the DWR can be reliably estimated using two radars with noncollocated beams and completely independent volume coverage patterns if the radar data are represented in the QVP/CVP format. The larger DWR is well correlated with the surface D_m (Fig. 3c) in agreement with Eq. (10). Note that we used the KASPR data collected at an elevation angle of 15°, which could result in approximately 10% variability in DWR–D_m relation.

Another remarkable feature is an almost perfect equivalence of the frequency-scaled K_{DP} values estimated by the two radars (Figs. 2c,d and 3b) which proves that the dominant contribution to K_{DP} is made by Rayleigh scattering size particles at the two very different radar wavelengths. This also

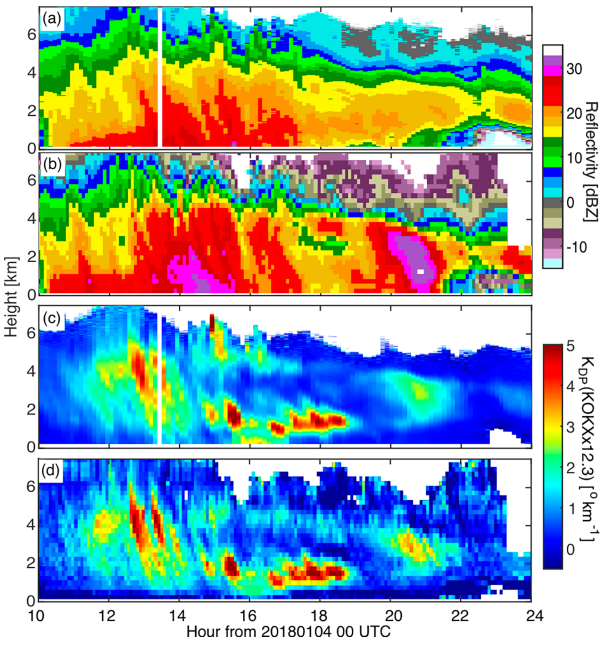

FIG. 2. Height vs time cross sections of the (a) KASPR Z QVP, (b) KOKX Z CVP, (c) KASPR K_{DP} QVP, and (d) KOKX K_{DP} CVP scaled by wavelength (multiplied by 12.3) for the case of 4 Jan 2018.

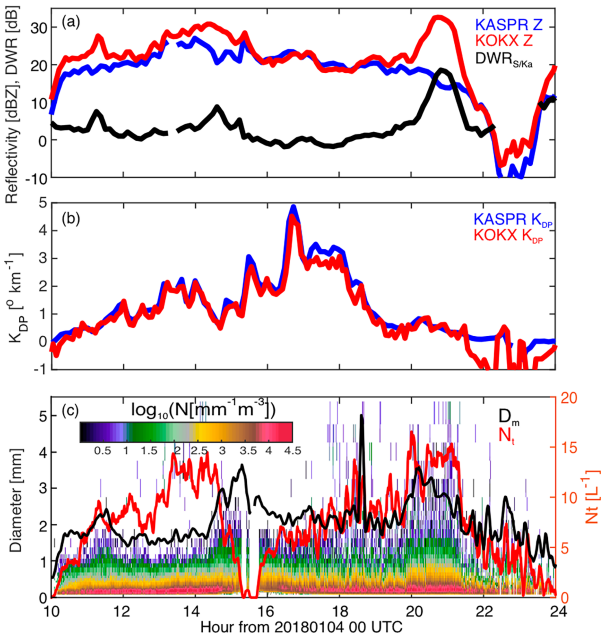

FIG. 3. Time series of (a) KASPR reflectivity (blue), KOKX reflectivity (red), and DWR$_{S/Ka}$ (black at 1 km height); (b) KASPR K_{DP} (blue) and KOKX K_{DP} scaled by wavelength (red) at 1-km height; and (c) Parsivel-measured PSD (color shade), D_m (black), and N_t (red) for the case of 4 Jan 2018.

suggests that the product $K_{DP}\lambda$ which is used in the retrieval equations discussed in section 3 is invariant with respect to the radar wavelength. The scatterplot of KASPR K_{DP} versus KOKX K_{DP} scaled by the wavelength ratio (multiplied by 12.27) generated from the data collected in all seven examined storms is displayed in Fig. 4b. Most of the data points are concentrated along the one-to-one line, and the correlation coefficient is higher than 0.9. The correlation is even higher if we consider only KASPR reflectivity values exceeding 18 dBZ. This suggests that the KASPR K_{DP} can be used for the estimation of the microphysical parameters of snow particles with Rayleigh scattering formulas. On the other hand, the CVP estimates of K_{DP} at the S band are good enough for quantification of snow although the magnitude of K_{DP} can be quite low.

Figure 5 shows examples of the height-versus-time cross sections of KASPR QVP and DWR$_{S/Ka}$ from the KOKX CVP and KASPR QVP for three different storms. Note that KOKX PPI volume coverage patterns did not always cover the entire cloud depth and are focused on the low levels (e.g., 2030–2130 UTC 16 December 2020), resulting in DWR$_{S/Ka}$ being available for regions where KOKX CVPs are available. KASPR QVPs show distinct K_{DP} fallstreaks originating from a dendritic-crystal growth layer (around −15°C, dashed lines in Figs. 5b,g,l), suggesting that the layer was seeded from the clouds aloft, and those ice particles' dendritic growth was facilitated, resulting in enhanced K$_{DP}$ (e.g., Bechini et al. 2013; Griffin et al. 2018). Large DWR$_{S/Ka}$ at lower levels corresponds to large D_m (>∼2 mm) at the surface (e.g., Figs. 5c,d 1430–1530, 2000–2130; Figs. 5h,i 2300–2530; and Figs. 5m,n 1530–1900 UTC). Generally, large DWR$_{S/Ka}$ (>∼10 dB) indicates that large snow aggregates are observed when KASPR K_{DP} is small (<1° km^{-1}) likely due to a low bulk density of large aggregates (e.g., Fig. 3c 2000–2130; Figs. 5b,c 2000–2130; Figs. 5g,h 2300–2500; and Figs. 5l,m 1000–1230, 1430–1600 UTC).

We found that the estimates of D_m from the Ka-band measurements seem to be more reliable for lower D_m (less than approximately 4 mm or lower DWR$_{S/Ka}$) compared to those for larger D_m (Figs. 5d,i,n). We evaluate the adaptation presented in section 3b. If the measurements from the S-band radar are available that can be matched with the Ka-band observations, then the Ka-band Z can be simply replaced with the S-band measurements, i.e., dBZ_{Ka} = dBZ_S − DWR$_{S/Ka}$ in all

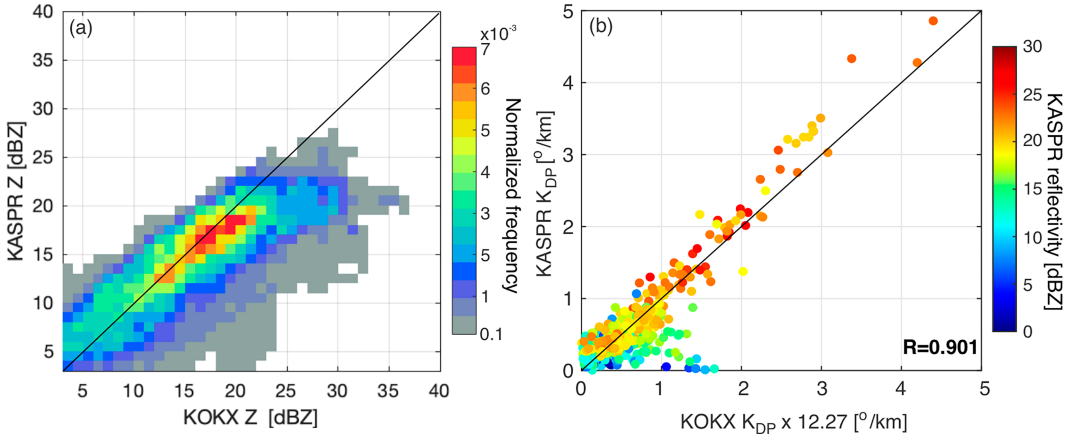

FIG. 4. (a) Frequency distribution of KASPR Z from the KASPR QVP and KOKX Z from the KOKX CVP from the seven selected cases. (b) KASPR K_{DP} from the KASPR QVP and KOKX K_{DP} from the KOKX CVP at 1-km height from the seven selected cases. KOKX K_{DP} was scaled by wavelength (multiplied by 12.3). Color shade in (b) represents the corresponding KASPR reflectivity. The correlation value R is displayed in (b). Black line in each panel represents a 1:1 line.

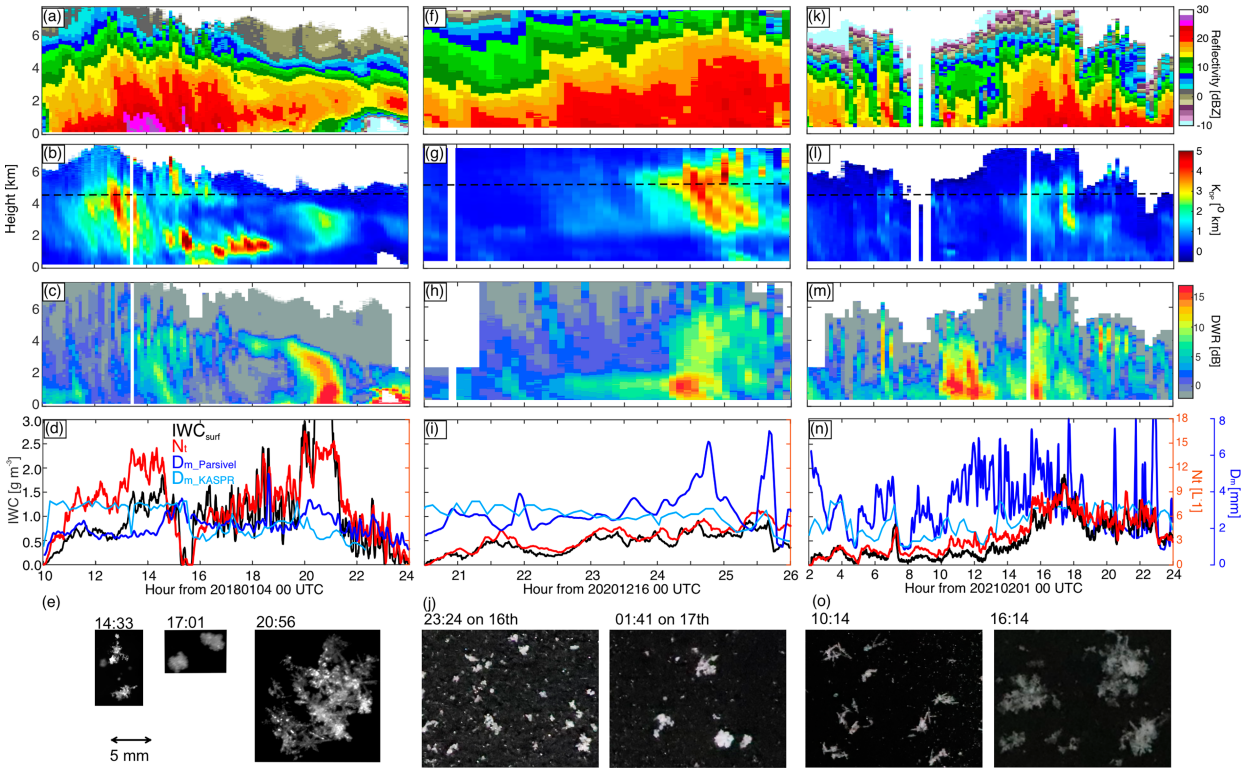

FIG. 5. Time-vs-height cross sections of (a),(f),(k) KASPR QVP reflectivity and (b),(g),(l) K_{DP}, and (c),(h),(m) $DWR_{S/Ka}$ from KASPR QVP and KOKX CVP; (d),(i),(n) time series of the surface IWC_{surf} (black line), N_t (red line), and D_m (blue line); and photos of snowflakes taken at the surface by (e) the MASC and (j),(o) the SLR camera. Dashed lines in (b), (g), and (l) represent the temperature of −15°C based on the nearest time soundings.

retrieval formulas for IWC(N_t, Z, μ) and IWC(K_{DP}, Z, f_{rim}). Our analysis of the joint KASPR and KOKX WSR-88D observations demonstrates that the use of relations where the Z_{Ka} corrections are made using D_m estimates is consistent with the Z_{Ka} corrections using $DWR_{S/Ka}$ measurements for the entire range of observed $DWR_{S/Ka}$ in this study ($0 < DWR_{S/Ka} < 16$ dB).

This technique can be particularly effective for stratiform, horizontally uniform precipitation within the QVP/CVP domain, which is quite common in the U.S. northeast coast winter storms. However, smaller-scale features that vary within the QVP/CVP domain, such as generating cells, convective cells, orographic-enhanced snow, and microphysical processes associated with those features, may not be adequately represented.

b. *Estimation of surface IWC, D_m, N_t, and f_{rim} from Parsivel and Pluvio*

The surface IWC (IWC_{surf}) is estimated using the Parsivel and Pluvio measurements. The estimation of the IWC requires knowledge of the particle density $\rho_s(D)$ as a function of the particle diameter D and of the third moment of the PSD, and it is determined as follows:

$$IWC = \frac{\pi}{6}\int_{D_{min}}^{D_{max}} \rho_s(D) D^3 N(D) dD, \tag{17}$$

where D is the equivolume diameter of the snowflake, ρ_s is its bulk density, and $N(D)$ is the size distribution of snowflakes. Here, we assume the inverse dependence of ρ_s on D parameterized by the degree of riming f_{rim} as specified by Eq. (3). Furthermore, we will use the Parsivel disdrometer to estimate the $N(D)$, and thus, the integral is replaced by a summation where n is the number of bins ($n = 32$) in a range from 0.062 to 24.5 mm in diameter as follows:

$$IWC = \frac{\pi}{6}\alpha_0 f_{rim}\sum_{i=1}^{n} D_i^2 N(D_i)\Delta D_i. \tag{18}$$

The degree of riming f_{rim} was estimated based on the combined use of the Parsivel $N(D)$ measurements and of the Pluvio precipitation flux or snow rate S measurement that is defined as follows:

$$S = 6\times 10^{-4}\frac{\pi}{\rho_w}\sum_i \rho_s(D_i) V_i^{(t)} D_i^3 N(D_i)\Delta D_i$$

$$= 6\times 10^{-4}\frac{\pi\alpha_0 f_{rim}}{\rho_w}\sum_i D_i^2 N_i^{(count)}, \tag{19}$$

where ρ_w is the density of water, and

$$N_i^{(count)} = V_i^{(t)} N(D_i)\Delta D_i, \tag{20}$$

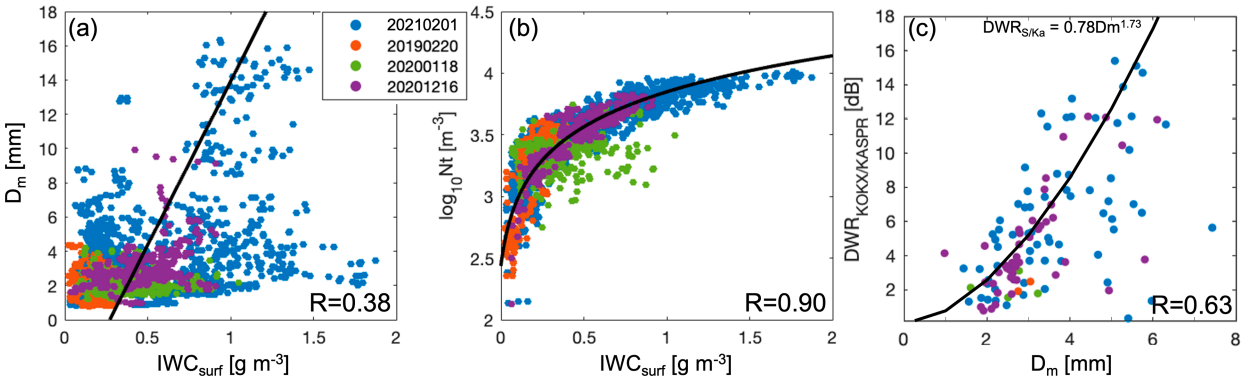

FIG. 6. (a) IWC_{surf} vs Parsivel D_m and (b) IWC_{surf} vs Parsivel N_t for the four snowstorm cases where Parsivel and Pluvio are both available. The color of the dots represents the dates. The black lines on (a) and (b) represent the linear regression line. (c) DWR from KOKX CVP and KASPR QVP (at 500 m height) vs Parsivel D_m. The black line on (c) represents Eq. (9). Each panel displays the correlation coefficient R.

which is the number of counts and fall velocity V_i for snow particles in the size bin ΔD_i directly measured by Parsivel. Therefore, the value of $f_{\rm rim}$ can be estimated as

$$f_{\rm rim} = \frac{S\rho_w}{6\times10^{-4}\pi\alpha_0\sum_i D_i^2 N_i^{(\rm count)}}. \tag{21}$$

Here, we should note that Parsivel's measurable diameter ranges from 0.062 to 24.5 mm. Battaglia et al. (2010) showed that Parsivel's small sampling volume could cause a decrease in the count of large snowflakes (>10 mm) in favor of smaller particles. They also showed that the Parsivel-measured particle size could be underestimated when the particles fell with canting angles $> 0°$. These could cause an error in estimating the integrated parameters in the equations above [Eqs. (16)–(21)].

For the other three cases (9 December 2017, 14 December 2017, and 4 January 2018) where Pluvio measurements were not available, we estimated the IWC_{surf} from the Parsivel measurements only by using $f_{\rm rim}$ estimates from the KASPR Doppler velocity measurements (section 4c). We use the median value of the $f_{\rm rim}$ estimates (1.63 for 9 December 2017, 1.17 for 14 December 2017, and 2.56 for 4 January 2018).

The mean volume diameter D_m was estimated as the ratio of the fourth and third moments of the particle size distributions. The total number concentration of snowflakes N_t was estimated via summation of all $N(D_i)$ measured by Parsivel. The estimated values of IWC (IWC_{surf}) and N_t from the surface measurements are shown in Figs. 5d, 5i, and 5n for the cases on 4 January 2018, 16 December 2020, and 1 February 2021. Our surface observations of those snowfall events indicate that IWC_{surf} is much better correlated with N_t than with D_m. This is clearly demonstrated in Fig. 6 where the scatterplots of IWC_{surf} versus D_m and IWC_{surf} versus N_t are presented for the cases on 20 February 2019, 18 January 2020, 16 December 2020, and 1 February 2021. The correlation coefficient between IWC_{surf} and N_t is 0.90 for the whole dataset, whereas the corresponding correlation coefficient between IWC_{surf} and D_m is only 0.38.

On the other hand, the Parsivel D_m and DWR from KOKX CVP and KASPR QVP follow Eq. (10) quite well (Fig. 6c). Moreover, D_m is well correlated with the radar reflectivity computed from the measured PSDs which is not surprising and agrees with the results of the study by Matrosov and Heymsfield (2017). In our dataset, the correlation coefficient between Z at the S band and D_m varies between 0.57 and 0.82 for different cases. We also noticed that the $K_{\rm DP}$ fallstreaks visible in Fig. 2c and Figs. 5b, 5g, and 5l are closely associated with high values of N_t and IWC_{surf} measured at the surface although such streaks most often do not reach the surface. This gives us a strong clue that the values of $K_{\rm DP}$ measured aloft may be used to estimate IWC and N_t at the surface.

c. *Estimation of f_{rim} from the radar measurements*

The estimates of N_t and IWC($K_{\rm DP}$, Z, $f_{\rm rim}$) are quite sensitive to the riming fraction $f_{\rm rim}$ (or rime mass fraction FR). We estimated FR and $f_{\rm rim}$ from the KASPR VPT Doppler velocity (DV) measurements using an FR–DV relation for the Ka band suggested by Kneifel and Moisseev (2020). Before the estimation, the vertical air motion component in DV was removed by estimating the mean DV of snowflakes as a function of Z using VPT data, following a technique proposed by Protat and Williams (2011) (details are also described in Oue et al. 2024). While DV also shows a dependence on reflectivity (Matrosov 2023), we neglect this dependence for the purpose of this study.

The estimated $f_{\rm rim}$ is averaged over 10 min at each height and then interpolated into the KASPR QVP space. The comparison of $f_{\rm rim}$ estimated from the KASPR DV and surface measurements [Eq. (21)] is illustrated in Fig. 7. The median value of the radar-estimated $f_{\rm rim}$ is 1.64 and that of the surface-measured $f_{\rm rim}$ is 1.83.

5. Evaluation and discussion

We apply the IWC(N_t, Z, μ) and IWC($K_{\rm DP}$, Z, $f_{\rm rim}$) estimates for seven snowfall events, but quantitative evaluation is available for the four cases where both Pluvio and Parsivel were operational (20 February 2019, 18 January 2020, 16 December 2020, and 1 February 2021). Figure 8 shows the

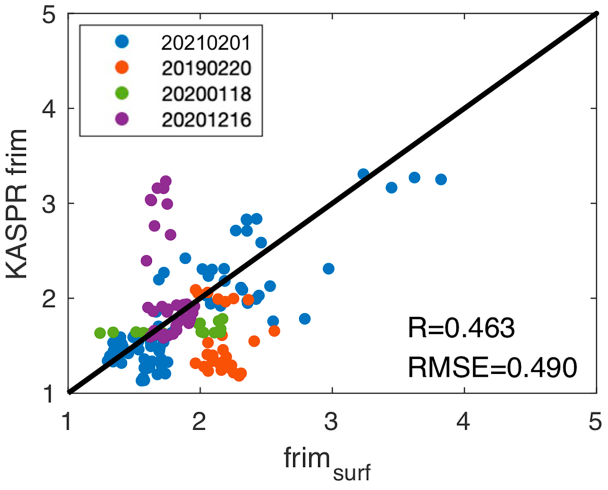

FIG. 7. The term f_{rim} estimated from the KASPR DV at the height of 500 m vs f_{rim} surface measurements using Eq. (21) for the four cases. The estimated f_{rim} from both KASPR and surface measurements is averaged over 10 min. Black line represents a 1:1 line.

time series of the retrieved and surface IWCs for the four cases, and Fig. 9 shows scatterplots for IWC(N_t, Z, μ) versus IWC_{surf} and IWC(K_{DP}, Z, f_{rim}) versus IWC_{surf}. In Fig. 8, the retrieved IWC is shifted in time so that the radar-estimated $D_m(K_{DP}, Z)$ and the Parsivel-measured D_m have the maximum correlation. Table 2 lists the median values of IWC_{surf} and the IWC estimates, their root-mean-square errors (RMSEs), and optimal μ values.

a. *Performance of the IWC(N_t, Z, μ) relation*

In the IWC(N_t, Z, μ) estimates, we assume that $f_{rim} = 2.0$ in Eq. (16) for all cases, which seems to be the average value of the riming degree for our dataset (see Fig. 7). As mentioned in section 3a(1), the proposed IWC(N_t, Z, μ) relation is less sensitive to f_{rim}.

The exponential PSD assumption ($\mu = 0$) for IWC(N_t, Z, μ) may not work for examined snow events. We optimized μ in such a way that the radar-estimated IWC(N_t, Z, μ) has the lowest RMSE when compared with the IWC_{surf}. Table 2 also lists the optimized μ value for each case. For five cases out of seven, the optimized μ is negative. Negative μ values are very common for winter snowstorm cases (e.g., Matrosov and Heymsfield 2017). Compared to the IWC(N_t, Z, μ) estimates using the different μ values, the use of $\mu = 0$ results in 1.3–2.7 times larger IWC(N_t, Z) than the use of the optimized μ for the negative μ cases and approximately 0.9 times of IWC(N_t, Z, μ) for the positive μ cases. Table 2 also lists the IWC(N_t, Z, μ) estimates and the RMSEs with the mean of the optimized μ value (-0.6). The average of the difference in the RMSE values between the use of the mean μ and the optimized μ approach is relatively small (0.049 g m^{-3}). Figure 9a shows a comparison of the radar IWC(N_t, Z, μ) estimates with the best μ estimates and IWC_{surf}. Overall, the IWC(N_t, Z, μ) estimates show a better agreement with IWC_{surf} than IWC(K_{DP}, Z, f_{rim}) (RMSE = 0.191 g m^{-3}, $R = 0.790$).

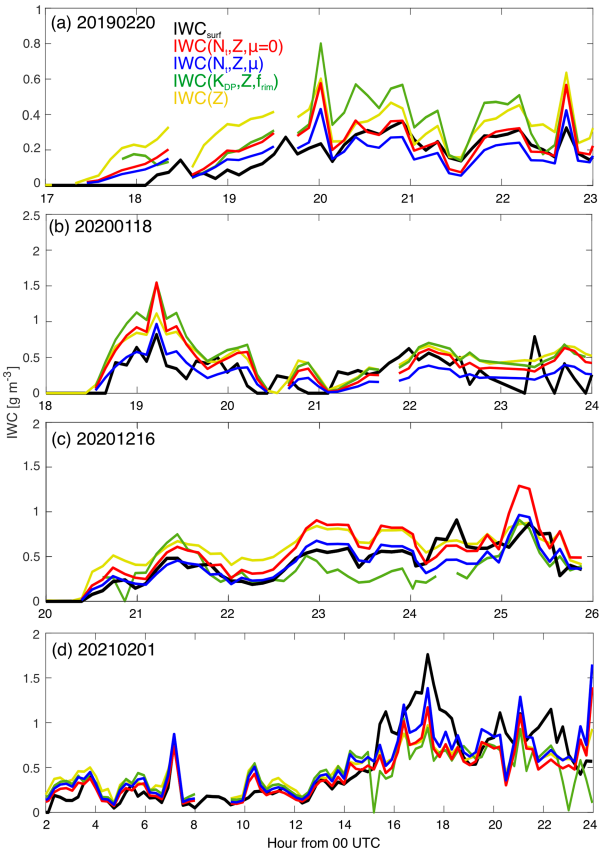

FIG. 8. Time series of IWC_{surf} (black) and the IWC estimates of IWC(N_t, Z) with $\mu = 0$ (red), IWC(N_t, Z, μ) with best estimates of μ (blue), IWC(K_{DP}, Z, f_{rim}) (green), and IWC(Z) from Matrosov and Heymsfield (2017) ($IWC = 0.038Z_{Ka}^{0.57}$, yellow) using the QVP data at 0.5-km height for (a) 20 Feb 2019, (b) 18 Jan 2020, (c) 16–17 Dec 2020, and (d) 1 Feb 2021. The retrieved IWC estimates are shifted in time so that the radar-estimated $D_m(K_{DP}, Z)$ and the Parsivel-measured D_m have the maximum correlation.

Figure 8 also displays the result for a simple IWC–Z relation ($IWC = 0.038Z_{Ka}^{0.57}$) proposed by Matrosov and Heymsfield (2017). This relation was derived from the microphysical sample data collected during the Global Precipitation Measurement Cold Season Precipitation Experiment (GCPEX), which was conducted in Canada during January–February of 2012. Fortuitously, the IWC(Z) estimate shows a good agreement with IWC_{surf}, suggesting that the snowfall in the GCPEX area (Ontario, Canada, near the Great Lakes) could be similar to our cases. The good agreement is particularly evident for IWC < 1 g m^{-3}. This is consistent with Matrosov and Heymsfield (2017) who showed that the IWC(Z) relationship is optimized for IWC $< \sim 0.6$ g m^{-3} (their Fig. 4a). It should be mentioned, however, that IWC(Z) relations generally exhibit significant variability depending on the datasets used to derive these relations (e.g., Matrosov and Heymsfield 2008). The IWC(N_t, Z, μ) estimate from the present study can improve the retrievals for larger IWC $> \sim 0.5$ g m^{-3}.

Tiira et al. (2016) reported a wider range of μ values ($-2 < \mu < 5$) than our cases, using surface in situ measurements

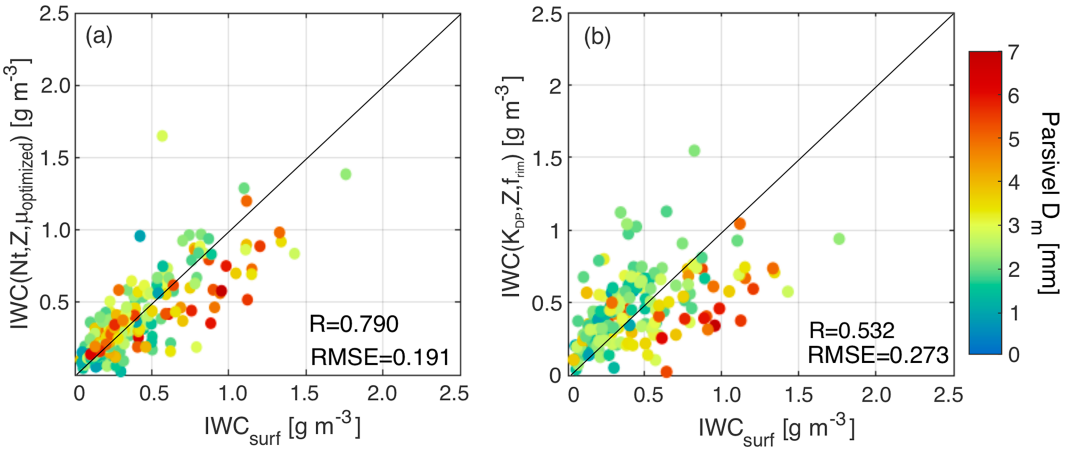

FIG. 9. (a) IWC(N_t, Z, μ) vs IWC_{surf} and (b) IWC(K_{DP}, Z, f_{rim}) vs IWC_{surf}. Color shades in (a) and (b) represent the Parsivel D_m. Black line in each panel represents a 1:1 line. The μ values are optimized for each case as shown in Table 2.

for 23 snow events in southern Finland. Our cases show μ values around -1 (Table 2) with the surface temperature near 0°C (Table 1), consistent with the previous studies (e.g., Matrosov and Heymsfield 2017). Those previous observations of μ also suggest a large variety of μ over short time intervals depending on cases and environments. We used a single value of μ for each case; however, instantaneous adjustment of μ may be needed for further improvements of the retrieval. Using better surface in situ measurements, estimating climatological values of μ depending on snow types would also help to improve the IWC(N_t, Z, μ) radar estimates.

b. *Performance of the IWC(K_{DP}, Z, f_{rim}) relation*

The performance of the IWC(K_{DP}, Z, f_{rim}) relation with f_{rim} estimated from the DV is illustrated in Figs. 8 and 9. In addition to the uncertainty associated with the insufficient representation of the surface measurements by the QVP and complex particle shapes as mentioned above, larger RMSE (0.273 g m^{-3}) compared to IWC(N_t, Z, μ) could be attributed to the uncertainty in the f_{rim} estimates (Fig. 7). Although the radar-estimated f_{rim} shows a good agreement with the surface-measured f_{rim} (Fig. 7), its variability could cause a larger error in the IWC estimate compared to the IWC(N_t, Z, μ) relation.

c. *Discussion on the performance of the suggested techniques and possible sources of errors*

There are multiple sources of errors that may affect the performance of the suggested relations for the estimation of IWC. One of them (and likely the most important) is uncertainty in the degree of riming f_{rim}. The f_{rim} dependencies are explicitly formulated in Eq. (16) for N_t and Eq. (7) for IWC(K_{DP}, Z, f_{rim}). Independent estimates of f_{rim} using a vertically pointing antenna are not always possible and reliable (Fig. 7).

The μ uncertainty is another important source of error. As opposed to f_{rim}, the value of μ cannot be directly estimated by the radar. Because K_{DP} is used for the estimation of D_m and IWC, the shape and orientation of ice particles and their natural variability may also have a prominent impact on the accuracy of our suggested methodology. Nevertheless, we believe that the optimal "climatological" values of such parameters as f_{rim} or μ can be obtained by matching the results of radar retrievals and in situ measurements after varying these

TABLE 2. The best estimate of μ and median values of the radar-estimated IWC_{surf} and the retrieved IWC(N_t, Z, μ) with the optimized μ, IWC(N_t, Z, μ) with $\mu = 0$, IWC(N_t, Z, μ) with $\mu = -0.6$, and IWC(K_{DP}, Z, f_{rim}) (g m^{-3}). The values in the parentheses for the retrieved IWC represent the RMSE based on IWC_{surf}. The median and RMSE values (g m^{-3}) for the retrievals are calculated using the data at the height of 0.5 km.

Case	μ	IWC_{surf} (g m^{-3})	IWC(N_t, Z, $\mu_{\text{optimized}}$) (g m^{-3})	IWC(N_t, Z, $\mu = 0$) (g m^{-3})	IWC(N_t, Z, $\mu = -0.6$) (g m^{-3})	IWC(K_{DP}, Z, f_{rim}) (g m^{-3})
9 Dec 2017 (no Pluvio)	−1.6	0.115	0.072 (0.065)	0.200 (0.257)	0.157 (0.178)	0.256 (0.249)
14 Dec 2017 (no Pluvio)	−1.2	0.142	0.105 (0.068)	0.194 (0.131)	0.152 (0.090)	0.345 (0.196)
4 Jan 2018 (no Pluvio)	0.3	0.974	0.530 (1.126)	0.484 (1.129)	0.381 (1.157)	0.398 (1.245)
20 Feb 2019	−0.7	0.202	0.166 (0.071)	0.221 (0.100)	0.212 (0.092)	0.310 (0.173)
18 Jan 2020	−1.0	0.394	0.307 (0.203)	0.490 (0.295)	0.470 (0.278)	0.568 (0.358)
16–17 Dec 2020	−0.7	0.479	0.430 (0.134)	0.575 (0.211)	0.552 (0.191)	0.323 (0.212)
1 Feb 2021	0.6	0.336	0.459 (0.237)	0.388 (0.255)	0.372 (0.263)	0.414 (0.295)

parameters in the retrieval algorithms. For example, based on the analysis of observational data, we came to the conclusion that estimates of IWC with the values of $f_{\text{rim}} = 2$ and slightly negative μ (with an average value of -0.6 for seven cases) work the best for the examined snow events that represent a typical snow type in the U.S. Northeast. Of course, these parameters may not be optimal for different types of snowstorms in other parts of the country, and a larger statistical dataset and a more comprehensive evaluation of the methodology are needed. Moreover, we evaluated the performance of our algorithms near the surface and not aloft, and an average climatological value of μ could be higher at lower temperatures (e.g., Heymsfield et al. 2013; Matrosov and Heymsfield 2017).

Both IWC(N_t, Z, μ) and IWC(K_{DP}, Z, f_{rim}) relations rely on the D_m estimates from KASPR. The radar-retrieved D_m sometimes does not follow peaks of the Parsivel D_m exceeding 4 mm (Figs. 5d,i,n) as discussed in section 4a, but this inconsistency does not seem to contribute to significant errors in the IWC estimates (e.g., 2330–2600 16 December 2020 and 1100–1800 UTC 1 February 2021 in Figs. 5 and 7). Overestimations with large spikes in the retrievals (e.g., 2000 and 2242 UTC 20 February 2019 and 1913 UTC 18 January 2020) are found when the retrieved D_m and measured DWR are inconsistent ($D_m > 3$ mm while DWR $< \sim 1$ dB). This may be caused by the radar sampling volume mismatch between the two radars, poorer representation of the surface measurements by the QVP, or complex particle shapes that are not taken into account in the derivation of the DWR–D_m relation.

6. Summary

The millimeter-wavelength polarimetric radars operating at the Ka and W microwave bands have been recently used for high-spatiotemporal-resolution observations of ice precipitation clouds. Much less attention was given to the quantification of ice/snow amounts in terms of IWC or precipitation rate using the millimeter-wavelength radars. Although the IWC estimates from centimeter-wavelength radars (e.g., operating at the S band) have been well established and evaluated in previous studies, those using millimeter-wavelength radars still have large uncertainties. In addition, many previously proposed IWC retrieval approaches using millimeter-wavelength radar measurements commonly utilize sophisticated scattering calculations that account for complex particle habits and densities; this might not be easily used for practical purposes. In this study, we propose novel methodologies for estimating IWC from Ka-band polarimetric radar measurements, which are evaluated using in situ surface measurements as well as Ka-band and S-band dual-frequency polarimetric radar observations. One technique prescribes a combined use of Z and K_{DP} with the degree of riming f_{rim} [the IWC(K_{DP}, Z, f_{rim}) relation], and another one implies the utilization of the IWC(N_t, Z, μ) relation, where N_t is polarimetrically retrieved. A key feature of both techniques is the introduction of a relationship between the DWR and mean volume diameter D_m ($\text{DWR}_{\text{S/Ka}} = 0.78D_m^{1.73}$) into the previously established IWC(K_{DP}, Z, μ) and IWC(N_t, Z) relations which implies the use of the "Rayleigh"-equivalent Z equal to its S-band value instead of the value of Z measured at the Ka band. Using the D_m(K_{DP}, Z) estimates, both techniques allow for single Ka-band radar measurements; i.e., $\text{DWR}_{\text{S/Ka}}$ measurements are not necessary.

We evaluated the two techniques via synergistic analysis of the data collected by the KASPR at Stony Brook, New York, and the neighboring NEXRAD (S-band) polarimetric radar at Upton, New York (KOKX), for seven snowstorms along the U.S. northeast coast. The KASPR polarimetric radar variables from the PPI measurements at 15° in elevation are converted to the QVPs, and the KOKX PPI measurements are converted to the CVPs averaged within a column with a 10 km × 10 km horizontal dimensions centered at the KASPR site with a vertical resolution of 50 m. The IWC estimates from the KASPR QVP are then evaluated with the surface IWC_{surf} obtained from the Parsivel and Pluvio weighing gauge measurements for four of the selected cases. The QVP and CVP methodologies for processing and displaying the data from the two neighboring radars allow for estimating DWR without the need for matching the radar beams and synchronizing scanning strategies for two noncollocated radars. The great benefit of utilizing millimeter-wavelength radars for the quantification of ice and snow is in the fact that K_{DP} at millimeter wavelengths is much higher than at a centimeter wavelength at which it can be quite low, noisy, and erratic in winter precipitation. The important conclusions from the study are listed herein.

- Significant DWR estimated from the KOKX CVP and KASPR QVP ($\text{DWR}_{\text{S/Ka}}$) indicates the presence of larger snowflakes (>15 mm in Parsivel-measured maximum dimension) and/or large mean volume diameter $D_m > 2$ mm. This suggests that the bulk $\text{DWR}_{\text{S/Ka}}$ retrieved from CVP/QVP can manifest the presence of larger particles although their radar beams do not match and such DWR can potentially be used for quantitative retrievals.
- The KOKX specific differential phase K_{DP} shows a good agreement with KASPR K_{DP} scaled by the wavelength ratio. This suggests that K_{DP} is primarily determined by smaller size ice particles that behave as Rayleigh scatterers at the S and Ka bands. On the other hand, it is also suggested that the KOKX K_{DP} has enough sensitivity for the quantification of small ice particles that are typically detected by the millimeter-wavelength radars which measure K_{DP} in a much larger dynamic range than the longer-wavelength radars. Generally, larger K_{DP} values are associated with low (near-zero) DWR, likely because K_{DP} is more sensitive to the number concentration of particles, while DWR is sensitive to larger particles.
- The term IWC_{surf} estimated from the Parsivel measurements more strongly depends on the total number concentration of particles N_t than on D_m. The IWC(N_t, Z, μ) relation for the Ka-band radar measurements is proposed using N_t estimated from Z, K_{DP}, and D_m or $\text{DWR}_{\text{S/Ka}}$ without the need for complex scattering calculations.
- The two IWC equations work quite well for ice/snow characterized by the mean volume diameter of particles D_m not

exceeding approximately 6 mm which encompasses a large majority of the snow events in the U.S. northeast. The KASPR-retrieved D_m sometimes does not capture peaks of the Parsivel D_m exceeding 4 mm, but this inconsistency does not contribute to significant errors in the IWC estimates. This illustrates that both techniques allow for single Ka-band radar measurements if D_m is reasonably estimated from the Ka-band radar observations. This works well for the entire range of observed $\mathrm{DWR_{S/Ka}}$ in this study ($0 < \mathrm{DWR_{S/Ka}} < 16$ dB). If snow is dominated by very large aggregates (i.e., large DWR), the use of DWR ($>\sim$17 dB) obtained from the measurements by a nearby centimeter-wavelength radar may be a better choice (if possible).

- The IWC(N_t, Z, μ) relation works well when the PSD parameter μ is between -1.6 and 0.6 (RMSE = 0.19 g m^{-3}, and the average value is -0.6).
- For the estimation using the IWC(K_{DP}, Z, f_{rim}) relation (RMSE = 0.27 g m^{-3}), optimization of the degree of riming f_{rim} is rather important and challenging. The vertically pointing radar Doppler velocity measurements can be used to estimate f_{rim}, and utilization of the median value of the estimated f_{rim} improves the performance of the IWC(K_{DP}, Z, f_{rim}) relation. The IWC(K_{DP}, Z, f_{rim}) could also depend on μ, which we did not take into account. The IWC(N_t, Z, μ) and IWC(K_{DP}, Z, f_{rim}) relations in this study may be differently affected by μ. The IWC(K_{DP}, Z, μ) can be further improved by incorporating the optimization of μ.
- While the IWC(N_t, Z, μ) estimates showed better RMSEs, the advantage of IWC(K_{DP}, Z, f_{rim}) technique is that it utilizes direct measurements of K_{DP} and Z, whereas a quite tricky procedure is needed for polarimetric retrieval of N_t. This suggests that the IWC(K_{DP}, Z, f_{rim}) technique may have a better potential for operational purposes if the error related to the f_{rim} estimate can be mitigated.

This study sheds light on the millimeter-wavelength polarimetric radar IWC estimation. Those techniques can be applied to other millimeter-wavelength radars if the DWR–D_m relation, which is obtained from a scattering calculation with simple assumptions about shape (spheroidal with an aspect ratio of 0.6) and size distribution (shape parameter $\mu = 0$), is adjusted to the wavelength and the measured K_{DP} is consistent with the Rayleigh assumption. This would be an easy-to-use technique compared to the techniques that require more sophisticated scattering calculations to represent complex snow particle shapes. However, the estimates in this study show some errors which may be primarily caused by the uncertainties in the degree of riming and the shape factor of the PSD approximated by the gamma function. Better surface in situ measurements (e.g., Precipitation Imaging Package, Newman et al. 2009; Tiira et al. 2016; Pettersen et al. 2020; Video In Situ Snowfall Sensor; Maahn et al. 2024) would help to better optimize μ and/or f_{rim} depending on the snow type to improve the IWC estimates. KASPR QVPs show distinct fallstreaks from a dendritic-crystal growth layer. The fallstreaks did not necessarily reach the surface but corresponded to large N_t and IWC at the surface. This suggests that the IWC(N_t, Z, μ) can be further improved by considering the microphysics (primary/secondary particle growth) and dynamics (e.g., wind shear) within the clouds.

Acknowledgments. This work was supported by the National Science Foundation (Oue and Kollias: AGS-1841215; 2113070), the National Aeronautics and Space Administration (Oue: LD80NSSC19K0394), and the U.S. Department of Energy (Matrosov: DE-SC0022163; Oue: DE-SC0021160). Funding for authors Ryzhkov and Bukovcic was provided by the NSF Grant AGS-1841246 and NOAA/Office of Oceanic and Atmospheric Research under NOAA–University of Oklahoma Cooperative Agreement NA21OAR4320204. Oue was partly supported by the SoMAS Seed Grant. We thank Dr. Sandra Yuter and Dr. Matthew Miller of North Carolina State University for providing multiangle snowflake camera data.

Data availability statement. The KASPR and sounding data used in this study are available at Stony Brook University Academic Commons Repository (https://commons.library.stonybrook.edu/somasdata/17). The data collected under IMPACTS (the data for the case of 18 January 2020) are also available at the NASA Global Hydrometeorology Resource Center (GHRC) DAAC system (http://dx.doi.org/10.5067/IMPACTS/RADAR/DATA101 and http://dx.doi.org/10.5067/IMPACTS/SOUNDING/DATA301).

REFERENCES

Aydin, K., and T. M. Walsh, 1999: Millimeter wave scattering from spatial and planar bullet rosettes. *IEEE Trans. Geosci. Remote Sens.*, **37**, 1138–1150, https://doi.org/10.1109/36.752232.

Battaglia, A., E. Rustemeier, A. Tokay, U. Blahak, and C. Simmer, 2010: PARSIVEL snow observations: A critical assessment. *J. Atmos. Oceanic Technol.*, **27**, 333–344, https://doi.org/10.1175/2009JTECHA1332.1.

Bechini, R., L. Baldini, and V. Chandrasekar, 2013: Polarimetric radar observations in the ice region of precipitating clouds at C-band and X-band radar frequencies. *J. Appl. Meteor. Climatol.*, **52**, 1147–1169, https://doi.org/10.1175/JAMC-D-12-055.1.

Botta, G., K. Aydin, J. Verlinde, A. E. Avramov, A. S. Ackerman, A. M. Fridlind, G. M. McFarquhar, and M. Wolde, 2011: Millimeter wave scattering from ice crystals and their aggregates: Comparing cloud model simulations with X- and Ka-band radar measurements. *J. Geophys. Res.*, **116**, D00T04, https://doi.org/10.1029/2011JD015909.

Bukovčić, P., D. Zrnić, and G. Zhang, 2017: Winter precipitation liquid–ice phase transitions revealed with polarimetric radar and 2DVD observations in central Oklahoma. *J. Appl. Meteor. Climatol.*, **56**, 1345–1363, https://doi.org/10.1175/JAMC-D-16-0239.1.

——, A. Ryzhkov, D. Zrnić, and G. Zhang, 2018: Polarimetric radar relations for quantification of snow based on disdrometer data. *J. Appl. Meteor. Climatol.*, **57**, 103–120, https://doi.org/10.1175/JAMC-D-17-0090.1.

——, ——, and ——, 2020: Polarimetric relations for snow estimation—Radar verification. *J. Appl. Meteor. Climatol.*, **59**, 991–1009, https://doi.org/10.1175/JAMC-D-19-0140.1.

Delanoë, J. M. E., A. J. Heymsfield, A. Protat, A. Bansemer, and R. J. Hogan, 2014: Normalized particle size distribution for remote sensing application. *J. Geophys. Res. Atmos.*, **119**, 4204–4227, https://doi.org/10.1002/2013JD020700.

Duffy, G., and D. J. Posselt, 2022: A gamma parameterization for precipitating particle size distributions containing snowflake aggregates drawn from five field experiments. *J. Appl. Meteor. Climatol.*, **61**, 1077–1085, https://doi.org/10.1175/JAMC-D-21-0131.1.

Garrett, T. J. and S. E. Yuter, 2014: Observed influence of riming, temperature, and turbulence on the fallspeed of solid precipitation. *Geophys. Res. Lett.*, **41**, 6515–6522, https://doi.org/10.1002/2014GL061016.

——, C. Fallgatter, K. Shkurko, and D. Howlett, 2012: Fall speed measurement and high-resolution multi-angle photography of hydrometeors in free fall. *Atmos. Meas. Tech.*, **5**, 2625–2633, https://doi.org/10.5194/amt-5-2625-2012.

Griffin, E. M., T. J. Schuur, and A. V. Ryzhkov, 2018: A polarimetric analysis of ice microphysical processes in snow, using quasi-vertical profiles. *J. Appl. Meteor. Climatol.*, **57**, 31–50, https://doi.org/10.1175/JAMC-D-17-0033.1.

Heymsfield, A. J., C. Schmitt, and A. Bansemer, 2013: Ice cloud particle size distributions and pressure-dependent terminal velocities from in situ observations at temperatures from 0° to −86°C. *J. Atmos. Sci.*, **70**, 4123–4154, https://doi.org/10.1175/JAS-D-12-0124.1.

——, S. Y. Matrosov, and N. B. Wood, 2016: Toward improving ice water content and snow-rate retrievals from radars. Part I: X and W Bands, emphasizing *CloudSat*. *J. Appl. Meteor. Climatol.*, **55**, 2063–2090, https://doi.org/10.1175/JAMC-D-15-0290.1.

Hogan, R. J., N. Gaussiat, and A. J. Illingworth, 2005: Stratocumulus liquid water content from dual-wavelength radar. *J. Atmos. Oceanic Technol.*, **22**, 1207–1218, https://doi.org/10.1175/JTECH1768.1.

——, M. P. Mittermaier, and A. J. Illingworth, 2006: The retrieval of ice water content from radar reflectivity factor and temperature and its use in evaluating a mesoscale model. *J. Appl. Meteor. Climatol.*, **45**, 301–317, https://doi.org/10.1175/JAM2340.1.

Huang, D., K. L. Johnson, Y. Liu, and W. J. Wiscombe, 2009: High resolution retrieval of liquid water vertical distributions using collocated Ka-band and W-band cloud radars. *Geophys. Res. Lett.*, **36**, L24807, https://doi.org/10.1029/2009GL041364.

Huang, G.-J., V. N. Bringi, D. Moisseev, W. A. Petersen, L. Bliven, and D. Hudak, 2015: Use of 2D-video disdrometer to derive mean density–size and Z_e–SR relations: Four snow cases from the light precipitation validation environment. *Atmos. Res.*, **153**, 34–48, https://doi.org/10.1016/j.atmosres.2014.07.013.

Huang, Y., and Coauthors, 2021: Microphysical processes producing high ice water contents (HIWCs) in tropical convective clouds during the HAIC-HIWC field campaign: Evaluation of simulations using bulk microphysical schemes. *Atmos. Chem. Phys.*, **21**, 6919–6944, https://doi.org/10.5194/acp-21-6919-2021.

Hubbert, J., and V. N. Bringi, 1995: An iterative filtering technique for the analysis of copolar differential phase and dual-frequency radar measurements. *J. Atmos. Oceanic Technol.*, **12**, 643–648, https://doi.org/10.1175/1520-0426(1995)012<0643:AIFTFT>2.0.CO;2.

IPCC, 2013: *Climate Change 2013: The Physical Science Basis*. Cambridge University Press, 1535 pp., https://doi.org/10.1017/CBO9781107415324.

Kneifel, S., and D. Moisseev, 2020: Long-term statistics of riming in nonconvective clouds derived from ground-based doppler cloud radar observations. *J. Atmos. Sci.*, **77**, 3495–3508, https://doi.org/10.1175/JAS-D-20-0007.1.

——, A. von Lerber, J. Tiira, D. Moisseev, P. Kollias, and J. Leinonen, 2015: Observed relations between snowfall microphysics and triple-frequency radar measurements. *J. Geophys. Res. Atmos.*, **120**, 6034–6055, https://doi.org/10.1002/2015JD023156.

Kollias, P., E. E. Clothiaux, M. A. Miller, B. A. Albrecht, G. L. Stephens, and T. P. Ackerman, 2007: Millimeter-wavelength radars: New frontier in atmospheric cloud and precipitation research. *Bull. Amer. Meteor. Soc.*, **88**, 1608–1624, https://doi.org/10.1175/BAMS-88-10-1608.

——, N. Bharadwaj, K. Widener, I. Jo, and K. Johnson, 2014a: Scanning ARM cloud radars. Part I: Operational sampling strategies. *J. Atmos. Oceanic Technol.*, **31**, 569–582, https://doi.org/10.1175/JTECH-D-13-00044.1.

——, and Coauthors, 2014b: Scanning ARM cloud radars. Part II: Data quality control and processing. *J. Atmos. Oceanic Technol.*, **31**, 583–598, https://doi.org/10.1175/JTECH-D-13-00045.1.

——, and Coauthors, 2020a: The ARM radar network: At the leading edge of cloud and precipitation observations. *Bull. Amer. Meteor. Soc.*, **101**, E588–E607, https://doi.org/10.1175/BAMS-D-18-0288.1.

——, E. Luke, M. Oue, and K. Lamer, 2020b: Agile adaptive radar sampling of fast-evolving atmospheric phenomena guided by satellite imagery and surface cameras. *Geophys. Res. Lett.*, **45**, e2020GL088440, https://doi.org/10.1029/2020GL088440.

Kumjian, M. R., and K. A. Lombardo, 2017: Insights into the evolving microphysical and kinematic structure of northeastern U.S. winter storms from dual-polarization Doppler radar. *Mon. Wea. Rev.*, **145**, 1033–1061, https://doi.org/10.1175/MWR-D-15-0451.1.

——, A. V. Ryzhkov, H. D. Reeves, and T. J. Schuur, 2013: A dual-polarization radar signature of hydrometeor refreezing in winter storms. *J. Appl. Meteor. Climatol.*, **52**, 2549–2566, https://doi.org/10.1175/JAMC-D-12-0311.1.

——, D. M. Tobin, M. Oue, and P. Kollias, 2020: Microphysical insights into ice pellet formation revealed by fully polarimetric Ka-band Doppler radar. *J. Appl. Meteor. Climatol.*, **59**, 1557–1580, https://doi.org/10.1175/JAMC-D-20-0054.1.

Leinonen, J., and D. Moisseev, 2015: What do triple-frequency radar signatures reveal about aggregate snowflakes? *J. Geophys. Res. Atmos.*, **120**, 229–239, https://doi.org/10.1002/2014JD022072.

——, and W. Szyrmer, 2015: Radar signatures of snowflake riming: A modeling study. *Earth Space Sci.*, **2**, 346–358, https://doi.org/10.1002/2015EA000102.

Löffler-Mang, M., and U. Blahak, 2001: Estimation of the equivalent radar reflectivity factor from measured snow size spectra. *J. Appl. Meteor. Climatol.*, **40**, 843–849, https://doi.org/10.1175/1520-0450(2001)040<0843:EOTERR>2.0.CO;2.

Löhnert, U., and Coauthors, 2015: JOYCE: Jülich Observatory for Cloud Evolution. *Bull. Amer. Meteor. Soc.*, **96**, 1157–1174, https://doi.org/10.1175/BAMS-D-14-00105.1.

Maahn, M., and U. Löhnert, 2017: Potential of higher-order moments and slopes of the radar Doppler spectrum for retrieving microphysical and kinematic properties of Arctic ice

clouds. *J. Appl. Meteor. Climatol.*, **56**, 263–282, https://doi.org/10.1175/JAMC-D-16-0020.1.

——, D. Moisseev, I. Steinke, N. Maherndl, and M. D. Shupe, 2024: Introducing the Video In Situ Snowfall Sensor (VISSS). *Atmos. Meas. Tech.*, **17**, 899–919, https://doi.org/10.5194/amt-17-899-2024.

Matrosov, S. Y., 1998: A dual-wavelength radar method to measure snowfall rate. *J. Appl. Meteor. Climatol.*, **37**, 1510–1521, https://doi.org/10.1175/1520-0450(1998)037<1510:ADWRMT>2.0.CO;2.

——, 2021: Polarimetric radar variables in snowfall at Ka- and W-band frequency bands: A comparative analysis. *J. Atmos. Oceanic Technol.*, **38**, 91–101, https://doi.org/10.1175/JTECH-D-20-0138.1.

——, 2023: Frozen hydrometeor terminal fall velocity dependence on particle habit and riming as observed by vertically pointing radars. *J. Appl. Meteor. Climatol.*, **62**, 1023–1038, https://doi.org/10.1175/JAMC-D-23-0002.1.

——, and A. J. Heymsfield, 2008: Estimating ice content and extinction in precipitating cloud systems from CloudSat radar measurements. *J. Geophys. Res.*, **113**, D00A05, https://doi.org/10.1029/2007JD009633.

——, and ——, 2017: Empirical relations between size parameters of ice hydrometeor populations and radar reflectivity. *J. Appl. Meteor. Climatol.*, **56**, 2479–2488, https://doi.org/10.1175/JAMC-D-17-0076.1.

——, A. V. Korolev, and A. J. Heymsfield, 2002: Profiling cloud ice mass and particle characteristic size from doppler radar measurements. *J. Atmos. Oceanic Technol.*, **19**, 1003–1018, https://doi.org/10.1175/1520-0426(2002)019<1003:PCIMAP>2.0.CO;2.

——, C. G. Schmitt, M. Maahn, and G. de Boer, 2017: Atmospheric ice particle shape estimates from polarimetric radar measurements and in situ observations. *J. Atmos. Oceanic Technol.*, **34**, 2569–2587, https://doi.org/10.1175/JTECH-D-17-0111.1.

——, M. Maahn, and G. de Boer, 2019: Observational and modeling study of ice hydrometeor radar dual-wavelength ratios. *J. Appl. Meteor. Climatol.*, **58**, 2015–2017, https://doi.org/10.1175/JAMC-D-19-0018.1.

——, A.V. Ryzhkov, M. Maahn, G. de Boer, 2020: Hydrometeor shape variability in snowfall as retrieved from polarimetric radar measurements. *J. Appl. Meteor. Climatol.*, **59**, 1503–1517, https://doi.org/10.1175/JAMC-D-20-0052.1.

——, A. Korolev, M. Wolde, and C. Nguyen, 2022: Sizing ice hydrometeor populations using the dual-wavelength radar ratio. *Atmos. Meas. Tech.*, **15**, 6373–6386, https://doi.org/10.5194/amt-15-6373-2022.

Moisseev, D. N., S. Lautaportti, J. Tyynela, and S. Lim, 2015: Dual-polarization radar signatures in snowstorms: Role of snowflake aggregation. *J. Geophys. Res. Atmos.*, **120**, 12 644–12 655, https://doi.org/10.1002/2015JD023884.

——, A. von Lerber, and J. Tiira, 2017: Quantifying the effect of riming on snowfall using ground-based observations. *J. Geophys. Res. Atmos.*, **122**, 4019–4037, https://doi.org/10.1002/2016JD026272.

Mroz, K., A. Battaglia, C. Nguyen, A. Heymsfield, A. Protat, and M. Wolde, 2021: Triple-frequency radar retrieval of microphysical properties of snow. *Atmos. Meas. Tech.*, **14**, 7243–7254, https://doi.org/10.5194/amt-14-7243-2021.

Murphy, A. M., A. Ryzhkov, and P. Zhang, 2020: Columnar vertical profile (CVP) methodology for validating polarimetric radar retrievals in ice using in situ aircraft measurements. *J. Atmos. Oceanic Technol.*, **37**, 1623–1642, https://doi.org/10.1175/JTECH-D-20-0011.1.

Newman, A. J., P. A. Kucera, and L. F. Bliven, 2009: Presenting the Snowflake Video Imager (SVI). *J. Atmos. Oceanic Technol.*, **26**, 167–179, https://doi.org/10.1175/2008JTECHA1148.1.

Oue, M., P. Kollias, A. Ryzhkov, and E. P. Luke, 2018: Towards exploring the synergy between cloud radar polarimetry and Doppler spectral analysis in deep cold precipitating systems in the Arctic. *J. Geophys. Res. Atmos.*, **123**, 2797–2815, https://doi.org/10.1002/2017JD027717.

——, ——, S. Y. Matrosov, A. Battaglia, and A. V. Ryzhkov, 2021: Analysis of the microphysical properties of snowfall using scanning polarimetric and vertically pointing multi-frequency Doppler radars. *Atmos. Meas. Tech.*, **14**, 4893–4913, https://doi.org/10.5194/amt-14-4893-2021.

——, B. A. Colle, S. E. Yuter, P. Kollias, P. Yeh, L. M. Tomkins, 2024: Microscale updrafts within northeast U.S. coastal snowstorms using high-resolution cloud radar measurements. *Mon. Wea. Rev.*, **152**, 865–889, https://doi.org/10.1175/MWR-D-23-0055.1.

Pettersen, C., and Coauthors, 2020: The Precipitation Imaging Package: Assessment of microphysical and bulk characteristics of snow. *Atmosphere*, **11**, 785, https://doi.org/10.3390/atmos11080785.

Protat, A., and C. R. Williams, 2011: The accuracy of radar estimates of ice terminal fall speed from vertically pointing Doppler radar measurements. *J. Appl. Meteor. Climatol.*, **50**, 2120–2138, https://doi.org/10.1175/JAMC-D-10-05031.1.

Ryzhkov, A. V., and D. S. Zrnić, 2019: *Radar Polarimetry for Weather Observations*. Springer International Publishing, 486 pp., https://doi.org/10.1007/978-3-030-05093-1.

——, ——, and B. A. Gordon, 1998: Polarimetric method for ice water content determination. *J. Appl. Meteor. Climatol.*, **37**, 125–134, https://doi.org/10.1175/1520-0450(1998)037<0125:PMFIWC>2.0.CO;2.

——, P. Zhang, H. Reeves, M. Kumjian, T. Tschallener, S. Troemel, and C. Simmer, 2016: Quasi-vertical profiles—A new way to look at polarimetric radar data. *J. Atmos. Oceanic Technol.*, **33**, 551–562, https://doi.org/10.1175/JTECH-D-15-0020.1.

——, ——, P. Bukovčić, J. Zhang, and S. Cocks, 2022: Polarimetric radar quantitative precipitation estimation. *Remote Sens.*, **14**, 1695, https://doi.org/10.3390/rs14071695.

Sekhon, R. S., and R. C. Srivastava, 1970: Snow size spectra and radar reflectivity. *J. Atmos. Sci.*, **27**, 299–307, https://doi.org/10.1175/1520-0469(1970)027<0299:SSSARR>2.0.CO;2.

Sinclair, V. A., D. Moisseev, and A. von Lerber, 2016: How dual-polarization radar observations can be used to verify model representation of secondary ice. *J. Geophys. Res. Atmos.*, **121**, 10 954–10 970, https://doi.org/10.1002/2016JD025381.

Stephens, G. L., S.-C. Tsay, P. W. Stackhouse Jr., and P. J. Flatau, 1990: The relevance of the microphysical and radiative properties of cirrus clouds to climate and climatic feedback. *J. Atmos. Sci.*, **47**, 1742–1753, https://doi.org/10.1175/1520-0469(1990)047<1742:TROTMA>2.0.CO;2.

Szyrmer, W., A. Tatarevic, and P. Kollias, 2012: Ice clouds microphysical retrieval using 94-GHz Doppler radar observations: Basic relations within the retrieval framework. *J. Geophys. Res.*, **117**, D14203, https://doi.org/10.1029/2011JD016675.

Tetoni, E., F. Ewald, M. Hagen, G. Köcher, T. Zinner, and S. Groß, 2022: Retrievals of ice microphysical properties

using dual-wavelength polarimetric radar observations during stratiform precipitation events. *Atmos. Meas. Tech.*, **15**, 3969–3999, https://doi.org/10.5194/amt-15-3969-2022.

Tiira, J., D. N. Moisseev, A. von Lerber, D. Ori, A. Tokay, L. F. Bliven, and W. Petersen, 2016: Ensemble mean density and its connection to other microphysical properties of falling snow as observed in southern Finland. *Atmos. Meas. Tech.*, **9**, 4825–4841, https://doi.org/10.5194/amt-9-4825-2016.

Tobin, D. M., and M. R. Kumjian, 2017: Polarimetric radar and surface-based precipitation-type observations of ice pellet to freezing rain transitions. *Wea. Forecasting*, **32**, 2065–2082, https://doi.org/10.1175/WAF-D-17-0054.1.

Tridon, F., A. Battaglia, and P. Kollias, 2013: Disentangling Mie and attenuation effects in rain using a K_a-W dual-wavelength Doppler spectral ratio technique. *Geophys. Res. Lett.*, **40**, 5548–5552, https://doi.org/10.1002/2013GL057454.

von Lerber, A., D. Moisseev, L. F. Bliven, W. Petersen, A.-M. Harri, and V. Chandrasekar, 2017: Microphysical properties of snow and their link to Z_e–S relations during BAECC 2014. *J. Appl. Meteor. Climatol.*, **56**, 1561–1582, https://doi.org/10.1175/JAMC-D-16-0379.1.

Zawadzki, I., W. Szyrmer, C. Bell, and F. Fabry, 2005: Modeling of the melting layer. Part III: The density effect. *J. Atmos. Sci.*, **62**, 3705–3723, https://doi.org/10.1175/JAS3563.1.

Zhu, Z., K. Lamer, P. Kollias, and E. E. Clothiaux, 2019: The vertical structure of liquid water content in shallow clouds as retrieved from dual-wavelength radar observations. *J. Geophys. Res. Atmos.*, **124**, 14 184–14 197, https://doi.org/10.1029/2019JD031188.